

# Self-Attention for Raw Optical Satellite Time Series Classification

Marc Rußwurm and Marco Körner

*Chair of Remote Sensing Technology,  
Department of Aerospace and Geodesy,  
Technical University of Munich  
Arcisstraße 21, 80333 Munich, Germany*

---

## Abstract

Deep learning methods have received increasing interest by the remote sensing community for multi-temporal land cover classification in recent years. Convolutional Neural networks that elementwise compare a time series with learned kernels, and recurrent neural networks that sequentially process temporal data have dominated the state-of-the-art in the classification of vegetation from satellite time series. In natural language processing, a third mechanism has emerged and is extensively employed for semantic information extraction from sequences of words and language modeling. This self-attention mechanism allows a neural network to selectively extract features from specific times in the input sequence thus suppressing non-classification relevant information. Today, self-attention based neural networks dominate the state-of-the-art in natural language processing but are hardly explored and tested in the remote sensing context.

In this work, we embed self-attention in the canon of deep learning mechanisms for satellite time series classification for vegetation modeling and crop type identification. We compare it quantitatively to convolution, and recurrence and test four models that each exclusively relies on one of these mechanisms. The models are trained to identify the type of vegetation on crop parcels using raw and preprocessed Sentinel 2 time series over one entire year. To obtain an objective measure we find the best possible performance for each of the models by a large-scale hyperparameter search with more than 2400 validation runs. Beyond the quantitative comparison, we qualitatively analyze the models by an easy-to-implement, but yet effective feature importance analysis based on gradient back-propagation that exploits the differentiable nature of deep learning models. Finally, we look into the self-attention transformer model and visualize attention scores as bipartite graphs in the context of the input time series and a low-dimensional representation of internal hidden states using t-distributed stochastic neighborhood embedding (t-SNE).

*Keywords:* Self-Attention, Transformer, Time Series Classification, Multitemporal Earth Observation, Crop Type Mapping, Vegetation Monitoring, Deep Learning

---

## 1. Introduction

Satellites observe the Earth's surface in regular temporal intervals. Often, data is provided free-of-charge to the public through initiatives like ESA's Copernicus Program. For instance, the Sentinel 2 multispectral satellites acquire data at up to 10m resolution in 13 spectral bands every two to five days. In 2018, an enormous amount of 7.76 TiB<sup>1</sup> Sentinel 2 data was published on a daily average. Still, only 7.6%<sup>2</sup> of all published images in 2018 were actually downloaded [1]. This means that 12 out of 13 published images remained unused. Similar figures can be drawn for the Sentinel 1, 3 and 5 missions. This is a clear sign that, despite claims in academia and industry, methods and principles of Big Data Analytics are hardly applied to their full potential in the field of Earth observation. The reasons for this low exploitation ratio are manifold. First, visual inspection of satellite images is still often the first step of data acquisition. Intermediate results must often be visually interpretable to be controlled by domain experts. Preprocessing steps, like atmospheric correction or manual or automatic cloud filtering, are ubiquitous in remote sensing. All of these processes require computational resources or visual inspection that scales poorly when applying methods at dense temporal or global spatial scales. This demonstrates the demand for methods that utilize the entire body of available satellite data

---

<sup>1</sup>1 TiB = 2<sup>40</sup>B

<sup>2</sup>62,317,329 published, 4,737,253 downloaded Sentinel 2 products in 2018

and, thus, requires minimal supervision by experts with region-specific expert knowledge. In principle, deep learning mechanisms are well-suited to approximate preprocessing-like mechanisms by jointly learning feature extraction and classification within one neural network topology using gradient backpropagation. Developing models that do not strictly require extensive data preprocessing are likely a key contribution to utilize all available published satellite data accordingly in the future. In the scope of this objective, we evaluate three deep learning mechanisms on four deep learning models on selectively available preprocessed and readily available raw satellite data.

Summarizing, the contributions of this work are two-fold:

- A large-scale evaluation of deep learning models on preprocessed and raw satellite data using three mechanisms, *i.e.*, convolution, recurrence, and self-attention, for crop type identification.
- A quantitative and qualitative analysis of self-attention in the context commonly used deep learning models for satellite time series classification.

## 2. Related Work

Even though satellite data is inherently multi-temporal, this temporal dimension has been a topical focus for vegetation-related applications for a long time [2, 3]. The limited availability of multi-temporal satellite data and the excessive computational demand for temporal stacks of large-scale satellite images impeded broad exploitation of the temporal dimension. Methods relied on separate feature extraction, *i.e.*, calculation of vegetation indices [4, 5, 6, 7, 8] with temporal statistics [4, 7, 9], and classification mechanisms, *e.g.*, with Random Forest Classifiers [7, 10, 6] or Support Vector Machines [11, 12, 13], as summarized by [14, 15]. Similarly, [16, 17] fit non-symmetric Gaussian curves to satellite time series. The parameters of these curves, *i.e.*, steepest ascent and descent, and their times coincide with key phenological characteristics, such as the onset of greenness or date of senescence, that allow detailed phenological analyses [18, 19] and can be used as distinctive features for classification [20, 21].

Early work on Artificial Neural Networks [22, 23] aimed at learning feature extraction and classification with a single dynamic model. Early success was achieved in handwritten digit recognition [24] with multi-layer neural networks trained with gradient descent. However, comparatively recent advances in parallel processing and data availability [25, 26] were necessary to outperform common feature extraction and classification pipelines in computer vision [27, 28, 29, 30, 31] and natural language processing [32, 33, 34] on a large scale. Following these developments, mono-temporal Earth observation approaches have adapted 2D convolutional neural networks from computer vision with great success [35, 36, 37, 38]. Methods from multi-temporal Earth observation [39, 40, 41, 42, 43, 44] adapted models from natural language processing. Here, recurrent neural networks [45], such as Long Short-Term Memory (LSTM) [46] or Gated Recurrent Units (GRU) [47] were commonly used in encode-decoder architectures [48] for generative prediction of words. In Earth observation, the encoder model was utilized for change detection [41, 42], and land cover [20] as well as crop type identification [39, 44, 49, 50]. To utilize both spatial and temporal features from the time series, combinations of convolutional layers with recurrent layers [43, 42] and convolutional-recurrent networks [51] have been explored and comprehensively compared in [49]. These recurrent neural network encoders can be augmented by soft-attention mechanisms, originally developed for machine translation [52], as tested in [44]. Recently, the light-weight time-convolutional feed-forward neural networks have shown to be a powerful alternative [53] and have achieved promising results in crop type identification [54]. While the state-of-the-art in remote sensing remains focused on convolutional and recurrent architectures, *self-attention* [32] in combination with unsupervised pre-training [33, 34] has started dominating the state-of-the-art in natural language processing. In the remote sensing context, self-attention has hardly been explored in the canon of existing work on a comparative analysis with recurrence and convolutional mechanisms.

## 3. Method

In this section, we introduce the notation throughout this work and provide background on convolution, recurrence and address self-attention before employing these mechanisms in four neural network topologies in Section 4.

A deep learning model  $f_{\Theta} : \mathcal{X} \mapsto \mathcal{Y}$  approximates a mapping from an input domain  $\mathcal{X}$  to a target domain  $\mathcal{Y}$ . These deep models are implemented by cascaded neural network layers that form a problem-agnostic, non-linear differentiable function. The parameters  $\Theta$  are determined by minimizing an objective function  $\mathcal{L}(y, f_{\Theta}(\mathbf{X}))$  that

quantifies the dissimilarity of ground truth labels  $\mathbf{y} \in \mathcal{Y}$  and the model predictions  $\hat{\mathbf{y}} = f_{\Theta}(\mathbf{X})$ . This objective function is minimized iteratively via mini-batch stochastic gradient descent

$$\Theta_{t+1} \leftarrow \Theta_t - \mu \mathbf{s}_t, \quad \text{with } \mathbf{s}_t = \frac{1}{N} \sum_{i=1}^N \frac{\partial}{\partial \Theta} \mathcal{L}(\mathbf{y}_i, f_{\Theta_t}(\mathbf{x}_i)) \quad . \quad (1)$$

The gradients  $\frac{\partial}{\partial \Theta} \mathcal{L}$  are averaged over a batch of size  $N$ , while the learning rate  $\mu$  determines the step size. This optimization scheme guarantees that the chosen parameters  $\Theta$  are optimal for the observed dataset and objective function.

Deep learning for time series classification aims learning the mapping  $\hat{\mathbf{y}} = f_{\Theta}(\mathbf{X})$  from a input time series  $\mathbf{X} \in \mathcal{X}^T = \mathbb{R}^{T \times D} = (\mathbf{x}_0, \mathbf{x}_1, \dots, \mathbf{x}_T)$  of individual measurements  $\mathbf{x}_t \in \mathbb{R}^D$  of  $D$  features to one of  $C$  classes. The classes are represented by the *one-hot* target vector  $\mathbf{y} \in \{0, 1\}^C$  where  $y_i \in \{0, 1\}$  indicates the class by zero or one. We denote the approximation of the target vector as  $\hat{\mathbf{y}} \in [0, 1]^C$ . A neural network is a non-linear and differentiable function  $f_{\Theta} = f_{\Theta_1}^{(1)} \circ f_{\Theta_2}^{(2)} \circ \dots \circ f_{\Theta_L}^{(L)}$  of  $L$  cascaded layers  $f_{\Theta_l}^{(l)}$ . Each layer  $f_{\Theta_l}^{(l)} : \mathbf{H}^{(l)} \xrightarrow{\Theta_l} \mathbf{H}^{(l+1)}$  is a non-linear transformation parameterized by  $\Theta_l$  and maps an input representation  $\mathbf{H}^l \in \mathbb{R}^{T \times D_h}$  to hidden features  $\mathbf{H}^{l+1} \in \mathbb{R}^{T \times D_h}$  that encode increasingly higher-level features. In time series classification, one of the following mechanisms are used to implement this non-linear mapping.

### 3.1. Fully Connected Layers

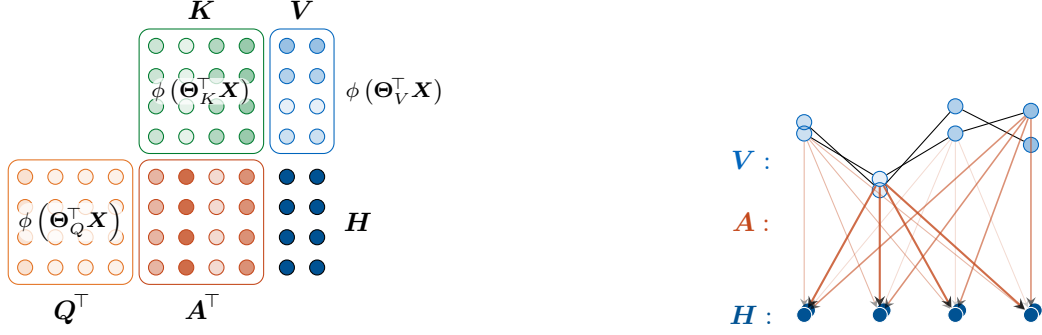
A dense or fully connected layer  $\mathbf{h}_t = f_{\Theta}^{\text{fc}}(\mathbf{x}_t) \in \mathbb{R}^{D_h}$  is applied at time instance  $t$  of a series independently. Each vector  $\mathbf{x}_t \in \mathbb{R}^D$  is transformed  $\mathbf{h}_t = f_{\{\Theta_1, \Theta_b\}}^{\text{fc}}(\mathbf{x}_t) = \phi\left(\Theta_1^{\top} \mathbf{x}_t + \Theta_b\right)$  by a linear transformation  $\Theta_1 \in \mathbb{R}^{D \times D_h}$  with optional bias-translation  $\Theta_b \in \mathbb{R}^{D_h}$  followed by a non-linear activation function  $\phi(\cdot) \in \{\tanh, \sigma, \text{ReLU}, \dots\}$ .

### 3.2. Recurrent Layers

Recurrent Neural Networks [55] extend fully connected layers by contextual information from previous times  $\mathbf{h}_{t-1}$ . This results in the transformation  $\mathbf{h}_t = f_{\Theta}^{\text{mn}}(\mathbf{x}_t, \mathbf{h}_{t-1}) = \phi\left(\Theta_x^{\top} \mathbf{x}_t + \Theta_h^{\top} \mathbf{h}_{t-1} + \Theta_b\right)$ . This formulation is prone to *vanishing* and *exploding* gradients through time [46, 56, 45, 57] that inhibited the extraction of features from long-term temporal contexts. While the effect of exploding gradients could be controlled through gradient clipping, vanishing gradients were addressed by the introduction of additional gates. This lead to *Long Short-Term Memory (LSTM)* recurrent networks [46] that introduced four internal gates  $\mathbf{f}_t = f_{\Theta_f}^{\text{mn}}(\mathbf{x}_t, \mathbf{h}_{t-1})$ ,  $\mathbf{i}_t = f_{\Theta_i}^{\text{mn}}(\mathbf{x}_t, \mathbf{h}_{t-1})$ ,  $\mathbf{g}_t = f_{\Theta_g}^{\text{mn}}(\mathbf{x}_t, \mathbf{h}_{t-1})$ ,  $\mathbf{o}_t = f_{\Theta_o}^{\text{mn}}(\mathbf{x}_t, \mathbf{h}_{t-1})$ . An additional *cell state* matrix  $\mathbf{c}_t$  was introduced as container for long-time temporal context. This cell state is updated at each iteration  $\mathbf{c}_t = \mathbf{f}_t \odot \mathbf{c}_{t-1} + \mathbf{i}_t \odot \mathbf{g}_t$  by element-wise multiplications  $\odot$  with the results of the forget  $\mathbf{f}_t$ , input  $\mathbf{i}_t$ , and modulation  $\mathbf{g}_t$  gates. The cell output  $\mathbf{h}_t = \mathbf{o}_t \odot \tanh(\mathbf{c}_t)$  is calculated using the result from the output gate  $\mathbf{o}_t$  and the new cell state  $\mathbf{c}_t$ . Overall, these transformations yield the long short-term memory update  $f_{\Theta}^{\text{lstm}} : \mathbf{h}_t, \mathbf{c}_t \leftarrow \mathbf{x}_t, \mathbf{h}_{t-1}, \mathbf{c}_{t-1}$ . An alternative to LSTMs are *gated recurrent units (GRUs)* [47] that follow the same principle of additional gates, but are parameterized with fewer gates and less weights. A empiric evaluation [58] did not show a significant difference in performance between these parameterizations.

### 3.3. 1D Convolutional Layers

Convolutional layers extract features from correlating a the input signal  $\mathbf{X} \in \mathbb{R}^{T \times D}$  with a set of  $D_h$  convolutional kernels  $\Theta = (\Theta_0, \Theta_1, \dots, \Theta_{D_h})$  with  $\Theta_d \in \mathbb{R}^{K \times D}$  by a convolutional operation  $\mathbf{H} = \phi(\mathbf{X} * \Theta)$  followed by an element-wise nonlinear activation function  $\phi$ . The size of the convolutional kernel  $K$  determines the receptive field of each layer. In contrast to recurrent layers, convolutional layers extract features from a fixed temporal neighborhood. The receptive field increases through the number of layers. Convolutional layers perform well in the field of computer vision where features from a local neighborhood of an image are extracted with small local kernel sizes. In a temporal context, larger kernel sizes are used where the learned kernel resembles a correlation with learned patterns in the time domain [59, 60] with recent application in remote sensing [54].



(a) visualization of the matrix multiplications involved in the calculation of attention scores  $\mathbf{A}$

(b) relationship between values and outputs drawn as bipartite graph

Figure 1: Schematic self-attention operation using  $T_{\text{in}} = T_{\text{out}} = 4$ ,  $D_{\text{in}} = D_{\text{out}} = 2$  and  $D_{\text{h}} = 4$ . The hidden output  $\mathbf{H} \in \mathbb{R}^{4 \times 2}$  results from matrix multiplication with attention scores  $\mathbf{A} \in [0, 1]^{4 \times 4}$  with a time series  $\mathbf{V} \in \mathbb{R}^{4 \times 2}$ . These attention scores themselves are calculated by a matrix multiplication between key  $\mathbf{K} \in \mathbb{R}^{4 \times 4}$  and query matrices  $\mathbf{Q} \in \mathbb{R}^{4 \times 4}$ . In self-attention, all key, query and value matrices originate from an input time series  $\mathbf{X}$  transformed via a linear mapping  $\mathbf{X}\Theta$  with a non-linear activation function  $\phi(\cdot)$

### 3.4. Self-Attention Layers

Attention mechanisms [52] allow a neural network to extract features from specific observation times of an input time series of values  $\mathbf{V} = (\mathbf{v}_0, \mathbf{v}_1, \dots, \mathbf{v}_{T_{\text{in}}}) \in \mathbb{R}^{T_{\text{in}} \times D_{\text{in}}}$ . This is realized by a weighted sum  $\mathbf{h}_i = \sum_{t=0}^{T_{\text{in}}} \alpha_t \mathbf{v}_t = \alpha^\top \mathbf{V}$  of attention scores  $\alpha \in [0, 1]^{T_{\text{in}}}$ ,  $\sum_i \alpha_i = 1$ . Extending this to a matrix multiplication

$$\mathbf{H} = \mathbf{A}^\top \mathbf{V} \quad (2)$$

with attention matrix  $\mathbf{A} = (\mathbf{a}_0, \dots, \mathbf{a}_{T_{\text{out}}})$  and  $\mathbf{H} = (\mathbf{h}_0, \dots, \mathbf{h}_{T_{\text{out}}}) \in \mathbb{R}^{T_{\text{out}} \times D_{\text{out}}}$ , calculates  $T_{\text{out}}$  output vectors in parallel. To illustrate these operations and to prepare for numerical results later in Section 8.3, we show a visual representation of these operations in Fig. 1. Attention scores themselves are the result of a second matrix multiplication of key  $\mathbf{K} \in \mathbb{R}^{T_{\text{in}} \times D_{\text{h}}}$  and query  $\mathbf{Q} \in \mathbb{R}^{T_{\text{out}} \times D_{\text{h}}}$  matrices. This results in the generic formulation of attention

$$\mathbf{H} = \underbrace{\text{softmax}(\mathbf{Q}\mathbf{K}^\top)}_{\mathbf{A}^\top} \mathbf{V} \quad (3)$$

that involves a softmax function to normalize  $\mathbf{A}$ . In self-attention [32]

$$\mathbf{H} = f_{\{\Theta_K, \Theta_Q, \Theta_V\}}(\mathbf{X}) = \text{softmax} \left( \frac{\phi(\Theta_Q^\top \mathbf{X}) \phi(\Theta_K^\top \mathbf{X})^\top}{\sqrt{D_{\text{h}}}} \right) \phi(\Theta_V^\top \mathbf{X}) \quad (4)$$

this formulation is adopted with unified dimensions  $D_{\text{in}} = D_{\text{out}} = D_{\text{h}}$  and  $T_{\text{in}} = T_{\text{out}}$  and the keys  $\mathbf{K} = \phi(\Theta_K^\top \mathbf{X})$ , queries  $\mathbf{Q} = \phi(\Theta_Q^\top \mathbf{X})$  and values  $\mathbf{V} = \phi(\Theta_V^\top \mathbf{X})$  matrices originate from the same input matrix  $\mathbf{X}$  transformed by three linear transformations with non-linear activation function  $\phi(\cdot)$ . Following the original work [32], the attention scores are scaled by  $\sqrt{D_{\text{h}}}$  for better gradient backpropagation. Today, self-attention mechanisms [32] are at the core of state-of-the-art natural language models [33, 34] and are experimentally analyzed later in Sections 8.3 and 8.4.

## 4. Models

The previous section provided an overview on neural network layers used for temporal feature extraction and introduced temporal convolution, recurrence, and self-attention. In this section, we describe four neural network

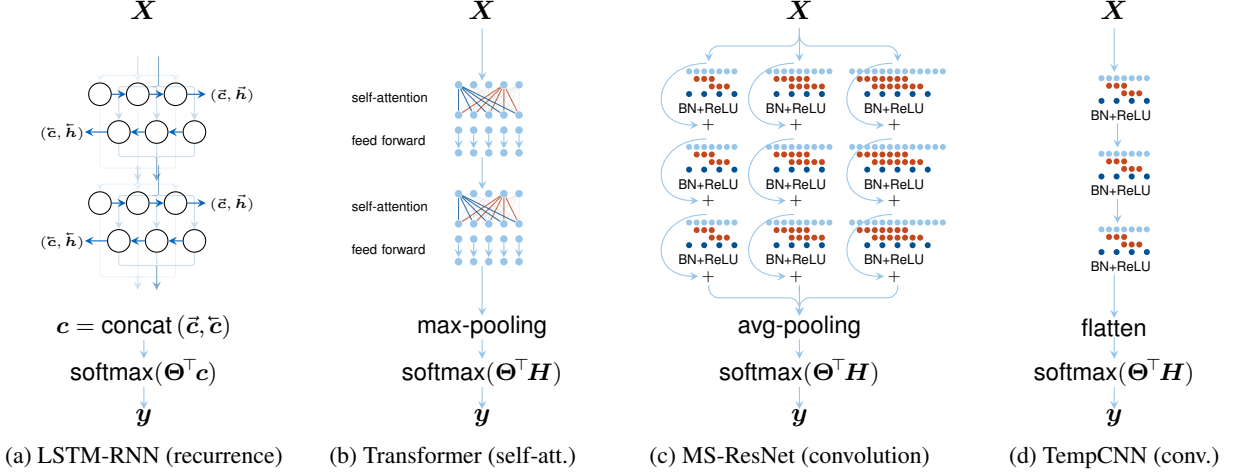


Figure 2: A schematic overview over the four network topologies used in this study.

topologies that each use one of these layer mechanisms and will be evaluated experimentally in the following<sup>3</sup>.

#### 4.1. Recurrent Long Short-Term Memory Neural Network

We designed a multi-layer *Recurrent Neural Network (RNN)* [55] with *Long Short-Term Memory (LSTM)*[46] cell architecture similar to our previous work [39]. This network encodes a satellite time series to increasingly higher-level  $D$ -dimensional representations through  $N$  cascaded bidirectional LSTM layers. The hidden states are initialized as zero-vectors. The last hidden states from forward  $\vec{c}$  and backward passes  $\bar{c}$  are concatenated and produce final classification scores via a dense output layer with softmax activation function. We schematically draw the network architecture in Fig. 2a We tuned the conditionality of hidden states  $D_h \in \{2^4, 2^5, \dots, 2^8\}$ , number of recurrent layers  $L \in \{1, 2, \dots, 7\}$  and applied dropout  $p_{\text{drop}} \in [0, 1]$  between the recurrent layers at training time.

#### 4.2. Transformer

For the self-attention model, we adopted the encoder architecture of the self-attention Transformer network [32], as illustrated in Fig. 2b. We discarded the step of word embedding, as the satellite time series data lives in a continuous space of spectral reflectance values. Following Vaswani *et al.* [32], we added a positional encoding to the time series, since self-attention can not utilize the sequential correlation of time series. Subsequently, the time series with positional encoding is transformed into higher-level  $D$ -dimensional feature representation through  $L$  transformer blocks. Each block encodes features through a multi-head self-attention mechanism followed by multiple dense layers applied to each time instance independently. Skip connections are implemented between the layers and layer normalization is used throughout the model. We refer to [32] for a detailed description of the layer topology. The representation of the last layer  $\mathbf{H} \in \mathbb{R}^{H \times T}$  is then reduced to  $\mathbf{h} \in \mathbb{R}^D$  by a global maximum pooling through the time dimension. This reduced representation is then projected to scores for each class by a final fully-connected layer with a softmax activation function.

For this architecture, we tune the dimensionality of the hidden states  $D_h \in \{2^4, 2^5, \dots, 2^8\}$ , the number of self-attention layers  $L \in \{1, 2, \dots, 8\}$ , and the number self attention heads  $H \in \{2, 3, \dots, 8\}$  that determine the number of self-attention mechanisms applied in parallel.

#### 4.3. Multi-Scale Residual Networks

*Residual Networks (ResNets)* [29] are an ubiquitous backbone architecture in computer vision. They consist of residual blocks  $f_{\Theta}^{\text{cbn}} = f_{\Theta}^c \circ f^b \circ f^r$  of convolution  $f_{\Theta}^c$  and batch normalization  $f^b$  [61] layers followed by a *Rectified Linear Unit (ReLU)* activation function  $f^r$ . Characteristically, in each block  $\mathbf{H} = f_{\Theta}^{\text{cbn}}(\mathbf{X}) + \mathbf{X}$  the encoded feature representation  $f_{\Theta}^{\text{cbn}}(\mathbf{X})$  is combined with the identity mapping of the input by addition. This forms residual skip

<sup>3</sup>The models are available at <https://github.com/marccoru/crop-type-mapping/tree/master/src/models>

connections where each residual layer numerically adds higher-level features to the forward propagated representation. These skip connections aid gradient backpropagation through the network and allow the training of very deep models.

These convolutional residual connections have been adopted to time series classification [62] where 2D convolutions through the spatial dimensions are replaced by 1D convolutions through time. Since convolutional layers, by design, extract features from the local (temporal) neighborhood, architectures that process time series at multiple scales [63] have shown good results on time series benchmark datasets [64, 65]. In this work, we utilize the architecture proposed by Wang ifnextchar. *et al.* ifnextchar, *et al.* [62]<sup>4</sup> where an input time series  $\mathbf{X} \in \mathbb{R}^{(T=512) \times D_{in}}$  is processed in three separate streams of each three residual blocks with increasing convolutional kernel sizes  $K^c \in \{3, 5, 7\}$ . Hence, each stream extracts features at a different temporal scale, as drawn in Fig. 2c. The representation after each stream is then average-pooled with pooling kernel sizes  $K^p \in \{16, 11, 6\}$  which yields three feature representations.  $\mathbf{h}^{K^c=3}, \mathbf{h}^{K^c=5}, \mathbf{h}^{K^c=7} \in \mathbb{R}^{D=256}$  and concatenated to a common representation  $\mathbf{H} \in \mathbb{R}^{D=768}$ . This vector is then reduced the activations per class by a final fully connected layer with softmax activation function. Note that the design of this network requires a fixed sequence length of  $T = 512$ . To obtain this sequence length, we interpolated the satellite time series by the nearest neighbor method. Since the architecture is precisely-defined in the original implementation, we solely tune the number of convolutional kernels  $D_h \in \{2^4, 2^5, \dots, 2^8\}$  for this architecture.

#### 4.4. TempCNN

Recently, the temporal convolutional network TempCNN [54] has been proposed and evaluated specifically for crop type mapping. It is a comparatively light-weight architecture of three sequential 1D convolutional layers followed by batch normalization, a ReLU activation function, and dropout. The encoded features are flattened and passed to a final fully connected layer with batch normalization, ReLU activation function, and dropout, as shown in Fig. 2d. These features are then projected to scores per class using a final fully connected layer and softmax.

The tune-able hyperparameters of this model are the number of convolutional kernels  $D_h \in \{2^4, 2^5, \dots, 2^8\}$  that determine the dimensionality of hidden states, the respective kernel sizes  $K \in \{3, 5, 7\}$ , and the dropout probability  $p_{drop} \in [0, 1]$ .

#### 4.5. Random Forest

As shallow learning baseline, we tested a *Random Forest (RF)* model using the `scikit-learn` framework [66]. We tuned the number of trees  $\{200, 400, \dots, 2000\}$ , the number of features to be considered at every split  $\{\text{auto}, \text{sqrt}\}$ , the maximum depth the the trees  $\{10, 20, \dots, 110\}$ , the minimum number of samples required to split a node  $\{2, 3, \dots, 10\}$ , the minimum number of samples required at each leaf node  $\{1, 2, 3, 4\}$ , and whether or not to use bootstrapping  $\{\text{true}, \text{false}\}$ .

## 5. Training Details

We trained the LSTM-RNN, MS-ResNet, TempCNN models via mini-batch stochastic gradient descent with gradients scaled using the Adam [67] optimizer with momentum parameters  $\beta_1 = 0.9$ , and  $\beta_2 = 0.98$ . The learning rate and weight decay parameters sampled from log-uniform distributions over  $[10^{-8}, 10^{-1}]$  and  $[10^{-12}, 10^{-1}]$ , respectively, and determined via hyperparameter tuning, as described in Section 6. Following Vaswani ifnextchar. *et al.* ifnextchar, *et al.* [32], we employed a learning rate scheduler for the Transformer model where the learning rate is first linearly increased for  $\text{warmup} = \{10^1, 10^2, 10^3\}$  gradient steps and reduced using exponential decay. We stopped the training early if the loss did not decrease over an average of the last 10 epochs. This condition must be true for five epochs in a row to stop the training process.

For the RF model baseline, we augmented the raw reflectance input features by additional spectral indices since feature extraction is usually required for a good performance of this model. Hence, we added the features *Normalized Difference Vegetation Index (NDVI)*, *Normalized Difference Water Index (NDWI)*, *Brightness Index (BI)*, *Inverted Red-Edge Chlorophyll Index (IRECI)*, and *Enhanced Vegetation Index (EVI)* to the time series data.

<sup>4</sup>Original implementation available at <https://github.com/geekfeiw/Multi-Scale-1D-ResNet>

## 6. Model Selection

The model architectures and training procedures required a variety of hyperparameters that may vary based on objective and dataset. We described the tuneable hyperparameters for each model in the previous sections. These were, for the deep learning models, the dimensionality of the hidden vectors, the number of layers, the number of self-attention heads, the convolutional kernel sizes, dropout probability, number of transformer warmup steps, learning rate, and weight decay. To determine the optimal set of parameters, we sampled candidate hyperparameters from a hyperparameter space, trained on a subset of the training partition, and evaluated the performance on a validation set. The partitioning scheme and spatial separation of the datasets is described in Section 7. Here, we first sampled hyperparameters from the search space at random for the first 34 models and recorded the validation performance measured in the kappa metric [68]. Based on these initial points, a kernel density function scaled by the validation performance of the model determined a probability distribution which was used to sample the next set of hyperparameters, following the protocol suggested by Bergstra *et al.* [69] and implemented using the HYPEROPT framework. We combined this with an *asynchronous successive halving* strategy [70]. This algorithm splits the 60 training epochs into four brackets with a grace period of 10 epochs. After each bracket, only the best-performing half of the models continued training, while the other runs were stopped at the end of each bracket. Both of these were implemented using the RAY-TUNE framework [71] that allowed hyperparameter training of four models in parallel per GPU on a NVIDIA-DGX1. For each model architecture, we evaluated on 300 sets of hyperparameters for both preprocessed and raw datasets which resulted in 2400 model evaluations.

The hyperparameters of the RF models were determined through a random search on 300 runs with three-fold cross-validation. To reduce tuning time and the class imbalance in the data, we used only up to 500 samples per class.

## 7. Data

We evaluated the mechanisms from Section 3 that are implemented in the models of Section 4 on the task of crop type identification. Crop type identification is a field of land cover and land use classification where the model has to extract classification-relevant features and learn a discriminative decision function to separate the classes of vegetation. We analyze the extracted features later in Section 8.4. Vegetation life cycle events, known as phenology, provides a distinctive temporal signal to identify types of vegetation using a limited set of spectral channels. This makes the temporal signal a key source of relevant features when learning a discriminative model to differentiate various types of vegetation and thus well-suited to test the mechanisms and models of this work.

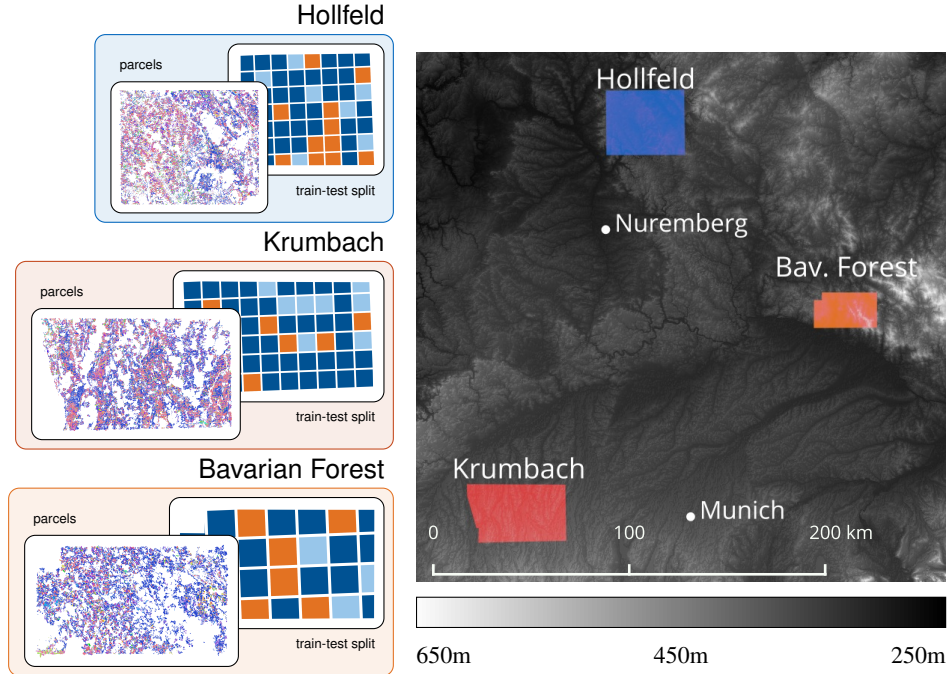
We focus on three spatially separate regions in Bavaria, as shown in Fig. 3. These regions are *Hollfeld* in Upper Franconia, *Krumbach* in Swabia, and a northeastern portion of the *Bavarian Forest*. These regions are located in approximately 100 kilometers distance from each other. While the climate is comparatively similar, different elevations and soil conditions favor differences in the distribution of cultivated crops, as can be observed in the class distribution histograms in Figs. 3b and 3c.

The label data for this study originates from a joint project with the *Bavarian State Ministry of Food, Agriculture and Forestry (StMELF)* and the German remote sensing company *GAF AG*. This enabled us to obtain two Sentinel 2 time series datasets from the same field parcels. One dataset with raw top-of-atmosphere Sentinel 2 observations acquired with minimal effort from Google Earth Engine, as described in Section 7.2.1, and one preprocessed time series dataset provided by *GAF AG* which can be considered prototypical for the industry-standard, as outlined in Section 7.2.2.

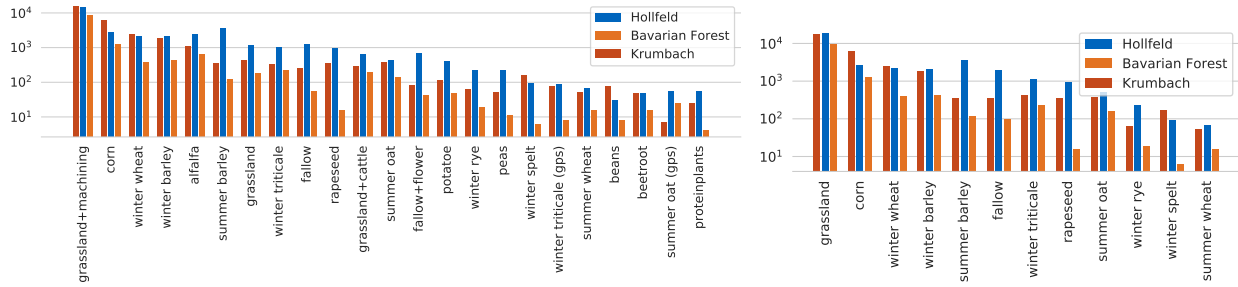
To get spatially separate partitions [72] for *training* of model parameters using gradient descent, *validation* of hyperparameter sets and final *evaluation* of the model, we divided the three regions further into rectangular blocks of 4500 by 4500 meters with a 500 meter margin between blocks, as shown in the train-test split in Fig. 3a. These blocks were randomly assigned to training, validation, and evaluation partitions in a 4:1:1 ratio. We decided for such a block-wise spatial separation in order to enforce independence of the dataset partitions without implicit overfitting, as experimentally evaluated and observed in previous work [39] and as recommended for geospatial data by further studies [73, 72] focusing the implicit bias of spatial auto-correlation.

### 7.1. Crop Type Labels

The *Common Agricultural Policy* of the European Union subsidizes farmers based on the type of cultivated crop. Each member country is required to gather geographical information of the geometry of the parcel and the type of crop. This information is provided by obligatory surveys as part of the subsidy application process directly from the



(a) The three areas of interest in Bavaria, Hollfeld, Krumbach and Bavarian Forest are located in different regional environments indicated by the elevation map. We show the field parcels colored by crop type, along with the random train test split for each of the regions.



(b) Class frequencies per region on a 23 class partition

(c) Class frequencies per region on 12 class partition

Figure 3: Test regions for labels and satellite time series

farmers. National agencies monitor the correctness either by gathering control samples on-site or by utilizing remote sensing and Earth observation technology.

The crop label categories provided for this study were provided by StMELF. They follow a *long-tailed class distribution* with over 269 distinct categories. Here, the most common 15, 26, and 62 categories cover 90%, 95%, and 99% of the field parcels, respectively. In cooperation with StMELF and GAF, a set of land-use and land-cover categories was aggregated and selected with respect to the aims and objectives of the ministry. From this aggregation, we selected two labeled datasets: The first contains 23 classes, as shown in Fig. 3b, which resemble the land-use of the parcels. These categories cover, for instance, multiple types of grassland. This dataset is a challenging to classify, since multiple categories (*e.g.*, grassland for cattle-use and for machining) share similar surface reflectance features measured by the satellite. We also aggregated the categories further a second dataset which focuses on 12 land cover categories, as shown in Fig. 3c. By evaluating models on two 23-class land-use categorization and 12-class land cover categorization, we aimed at reporting model accuracies from two differently difficult objectives.

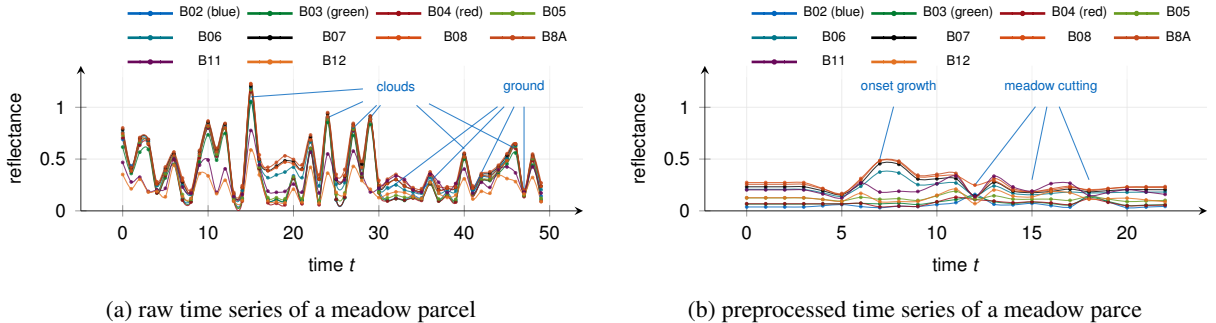


Figure 4: An illustration and comparison of a raw and a preprocessed Sentinel 2 time series of the same meadow field parcel. Preprocessing allows for a visual interpretation. The onset of growth after timestep  $t = 5$  is clearly visible. Also, several cutting events can be observed over the time of the vegetation period. The preprocessed time series, however, contains repeated values due to temporal interpolation and cloud removal. In the raw time series, most information from the measured signal is retained. Noise caused by, *e.g.*, atmospheric effects and clouds, obscures the phenological events.

## 7.2. Satellite Data

We utilized data from the optical Sentinel 2 satellite constellation which consists of two satellites that orbit the Earth on a sun-synchronous orbit on opposite tracks. These satellites observe the same spot on the Earth’s surface every 2 to 5 days, depending on the latitude. The data is gathered by a line-scanner at 13 spectral bands ranging from ultra-violet wavelengths, for capturing atmospheric water vapor, over optical and near-infrared wavelengths, sensitive to chlorophyll and photosynthesis, up to short-wave infrared wavelengths, which are sensitive to soil moisture. In regions where the sensor stripes overlap, we observed approximately 140 measurements of the same point during the entire year of 2018, while on the stripe centers we only recorded 70 observations within the same time range.

### 7.2.1. Raw Dataset

For the raw Sentinel 2 dataset, we utilized the *top-of-atmosphere* reflectances of the processing level L1C. This data was acquired from *Google Earth Engine* [74] and queried for each field parcel individually. Pixels located within the boundaries of a field parcel were mean-aggregated into a single feature vector of 13 spectral bands at each time. We show examples of a meadow parcel of the raw Sentinel 2 time series in Fig. 4a. Note that cloud coverage, visible as positive peaks in the reflectance profiles, dominates the signal and makes a visual interpretation of this time series difficult. This time series dataset is challenging to classify but can be acquired at minimal effort. Hence, we benchmarked our models on this harder objective.

### 7.2.2. Preprocessed Dataset

For further evaluation, we had access to a second dataset which originates from the same publicly available top-of-atmosphere data products. In contrast to the raw data set, this data was processed by GAF through their tested and operational preprocessing engine. This process includes common preprocessing techniques, such as, *e.g.*, atmospheric correction, temporal selection of cloud-free observations, a focus on observations of the vegetative period, and cloud masking. We show an example of the preprocessed dataset in Fig. 4b that shows the identical parcel as Fig. 4a. Here, the cloudy observations have been identified and filtered by a separate cloud classification model. This makes this dataset easier to classify by shallow models, as distinctive phenological features, *i.e.*, onset of growth and cutting of the meadows, can be visually distinguished. Overall, this preprocessing pipeline can be considered prototypical for an industry standard but requires significant computational and design effort to generate.

## 8. Experiments and Results

In this section, we experimentally compare the transformer model, that is based on self-attention, to a recurrent neural network and two convolutional neural networks, as described in Section 4. This experimental section is structured in three parts: First in Section 8.1, we show quantitative results on all evaluated neural network architectures.

Table 1: Comparison of models on preprocessed (pre) and raw dataset on the 23-class land use and the 12-class land cover categorization. The values reported are the mean and standard deviation of three models with the best, second and third-best hyperparameter sets trained on the training and validation partitions and tested on the evaluation partition.

(a) Kappa metric 23-class dataset						(b) Kappa metric 12-class dataset					
$\kappa$	RF	LSTM-RNN	Transformer	MS-ResNet	TempCNN	$\kappa$	RF	LSTM-RNN	Transformer	MS-ResNet	TempCNN
pre	0.76	0.78 $\pm$ 0.01	0.79 $\pm$ 0.03	0.76 $\pm$ 0.03	0.80 $\pm$ 0.00	pre	0.86	0.87 $\pm$ 0.01	0.87 $\pm$ 0.04	0.85 $\pm$ 0.01	0.88 $\pm$ 0.03
raw	0.53	0.71 $\pm$ 0.01	0.71 $\pm$ 0.03	0.69 $\pm$ 0.03	0.67 $\pm$ 0.02	raw	0.62	0.83 $\pm$ 0.01	0.82 $\pm$ 0.02	0.78 $\pm$ 0.02	0.71 $\pm$ 0.07

(c) Overall accuracy metric 23-class dataset						(d) Overall accuracy metric 12-class dataset					
acc.	RF	LSTM-RNN	Transformer	MS-ResNet	TempCNN	acc.	RF	LSTM-RNN	Transformer	MS-ResNet	TempCNN
pre	0.83	0.85 $\pm$ 0.01	0.85 $\pm$ 0.02	0.83 $\pm$ 0.02	0.86 $\pm$ 0.00	pre	0.91	0.92 $\pm$ 0.01	0.92 $\pm$ 0.03	0.91 $\pm$ 0.01	0.92 $\pm$ 0.02
raw	0.71	0.81 $\pm$ 0.01	0.80 $\pm$ 0.02	0.79 $\pm$ 0.03	0.79 $\pm$ 0.00	raw	0.80	0.90 $\pm$ 0.00	0.89 $\pm$ 0.01	0.87 $\pm$ 0.01	0.83 $\pm$ 0.04

(e) Class-mean $f_1$ score 23-class dataset						(f) Class-mean $f_1$ score 12-class dataset					
$f_1$	RF	LSTM-RNN	Transformer	MS-ResNet	TempCNN	$f_1$	RF	LSTM-RNN	Transformer	MS-ResNet	TempCNN
pre	0.38	0.47 $\pm$ 0.02	0.50 $\pm$ 0.06	0.49 $\pm$ 0.03	0.50 $\pm$ 0.02	pre	0.55	0.60 $\pm$ 0.02	0.66 $\pm$ 0.07	0.64 $\pm$ 0.02	0.60 $\pm$ 0.06
raw	0.18	0.43 $\pm$ 0.01	0.45 $\pm$ 0.06	0.44 $\pm$ 0.01	0.36 $\pm$ 0.01	raw	0.34	0.63 $\pm$ 0.01	0.64 $\pm$ 0.07	0.55 $\pm$ 0.04	0.41 $\pm$ 0.07

Here, we present results on preprocessed and raw Sentinel 2 data described in Section 7.2 and on two sets of categories. One 23-class categorization evaluates model performance on land use classification while the other 12-class categorization focuses on land cover. Next in Section 8.2, we analyze the ability of the models to suppress noise, *e.g.*, induced by clouds, in raw time series data by a feature importance analysis based on gradient backpropagation. Finally in Sections 8.3 and 8.4, we focus specifically on the self-attention mechanism and analyze activation scores and internal states of the transformer model in detail.

### 8.1. Quantitative Model Evaluation

We compared the performance of the deep learning models LSTM-RNN [46], Transformer [32], MS-ResNet [62], and TempCNN [54], as well as a Random Forest (RF) classifier as shallow baseline. We determined the optimal hyper-parameters separately for preprocessed and raw Sentinel 2 time series datasets, and for the 23 and 12 class categorizations, as described in Section 6. For each experiment, we trained and evaluated three different models with the best, second-best, and third-best hyperparameter configuration and random seeds for parameter initialization and composition of the training batches. In Table 1, we present the mean and standard deviation of the accuracy metrics from these three results. All models were trained and evaluated on block partitions for training and evaluation (*cf.* 3) in all three regions Hollfeld, Krumbach and Bavarian forest. We evaluated these models on raw and preprocessed satellite time series on identical field parcels.

It is noteworthy that the overall accuracy measure, as presented in Tables 1c and 1d, over-represents frequent classes. Since the datasets used for this study show a heavily imbalanced class distribution, the accuracy of frequent classes dominates this metric. Nevertheless, it is an intuitive measure and a good representation of the example-wise accuracy, representative of the visual impression from observing a spatial map classification. To account for the less frequent classes, we also report Cohen’s kappa metric [68] in Tables 1a and 1b. This is a correlation score that is frequently used in remote sensing and normalizes the classification scores by the probability of a random chance prediction based on empirical class frequencies. As a further measure of performance, we report the  $f_1$  score, *i.e.*, the harmonic mean of precision and recall, for each class and average over all classes in Tables 1e and 1f. By doing so, all classes get equally weighted disregarding the the number of samples per category. The class-mean  $f_1$  scores are generally lower than accuracy and kappa, as we chose a large set of classes where some classes semantically overlap or only have few examples which make it difficult for a data-driven neural network to learn feature extraction and decision function. Overall, we aimed at comparing different properties of the classification models. Hence, the overall

accuracy reflects the classification accuracy per field parcel, while the  $f_1$  score measures the accurate classification of all classes.

Table 1 reveals that data preprocessing had a positive effect on the accuracy,  $f_1$  score, and kappa of all models. It seems that the manual supervision during preprocessing improved the classification performance. This better performance on pre-processed time series is, to a certain degree, expected, since this preprocessing makes a visual identification of classification relevant events possible, as could be seen in Fig. 4b. Comparing the visual examples at 4 suggests that the classification of the preprocessed datasets is an easier task than approximating preprocessing-like mechanism jointly together with classification in a holistic end-to-end model. Overall, the region- and domain-specific expertise needed to design such preprocessing pipelines increases the classification performance compared to classification of the raw datasets were the deep learning models have to learn preprocessing-like mechanisms solely based on the provided examples without access to model knowledge. This holds especially true if the number of samples is limited, some examples are falsely labeled, or the semantic representation of classes do overlap. Considering this, it is notable that the LSTM-RNN and Transformer models performed competitively well on raw data compared to pre-processed data. Especially in the 12-class land cover categorization setting, the difference in performance was rather minor, speaking of 5% in accuracy and 0.03 in kappa score. In terms of the  $f_1$  score, the LSTM-RNN variant even achieved better performance on raw data compared to preprocessed data, while is ranging behind the Transformer. Throughout both the 23-class dataset (*cf.* Tables 1a, 1c and 1e) and 12-class dataset (*cf.* Tables 1b, 1d and 1f) variants, all evaluated deep learning models performed similarly well on preprocessed data. Interestingly, for the raw dataset partitions, the LSTM-RNN and Transformer models achieved slightly better accuracy, kappa, and  $f_1$  scores values compared to the MS-ResNet and TempCNN variants. In the 23-class setting, the difference is rather small with 1–2% in overall accuracy and 0.01 in kappa score which seems not significant considering their reported variances. The 12-class case, however, confirms this observation with a more pronounced difference of 0.03–0.07 in kappa metric and 5% and 11% in accuracy. In the next Section 8.2, we will investigate this further by a feature importance analysis monitoring the backpropagation process.

When comparing the  $f_1$  scores in Tables 1e and 1f with the accuracy scores in Tables 1c and 1d on raw data, we see that the convolutional TempCNN model showed similar performance compared to the MS-ResNet model. The  $f_1$  scores, however, show a lower score for TempCNN. From these metrics, we can derive that the TempCNN did classify the majority of field parcels accurately but achieved lower accuracies on some of the more infrequent class categories compared to MS-ResNet. This may be attributed to the shallower network topology.

Interestingly, the random forest baseline achieved competitive results to the deep learning models on preprocessed time series data. It appears that preprocessing, as a form of feature extraction, helped the random forest classifier to improve its performance significantly. Without data preprocessing on the raw dataset, the random forest baseline fell massively behind the deep learning models. The overall accuracy on pre-processed data was only 9% worse which hints toward a generally accurate classification of the most frequent classes. The kappa metric—that ranged 0.15 worse in the 23-class land use variant and 0.1 to 0.2 worse in the 12-class land use variant—indicates that infrequent classes were classified less accurately by the random forest classifier. This got further confirmed by the poor  $f_1$  score throughout both dataset variants where the random forest achieved worse performance on raw datasets compared to preprocessed datasets. Overall, this stresses the necessity of feature extraction for shallow machine learning methods while demonstrating that—with sufficient manual effort in preprocessing and, thus, feature extraction—random forests can achieve competitive accuracies.

It may be concluded that the region- and domain-specific expert knowledge in data preprocessing helped all models to achieve better accuracies compared to the raw sentinel 2 time series dataset. All models achieved similar accuracies for preprocessed datasets. Even the random forest classifier showed a competitive performance to the deep learning models with similar scores in overall accuracy, slightly worse kappa and  $f_1$  scores. Both, the LSTM-RNN and Transformer models, that rely on recurrence and self-attention, achieved better accuracies on raw time series data compared to the convolutional models MS-ResNet and TempCNN. This effect was minor in the land-use categorization with 23-classes and more pronounced in the land-cover categorization, but overall consistent throughout this evaluation. We will investigate the difference of recurrence and self-attention compared to convolution further in the next section.

## 8.2. Temporal Feature Importance Assessment by Gradient Backpropagation

In the previous section, we observed that models based on recurrence and self-attention achieved better accuracy metrics on noisy raw data compared to convolutional models. Here, we investigate this further through a simple, yet effective, feature importance analysis based on gradient backpropagation.

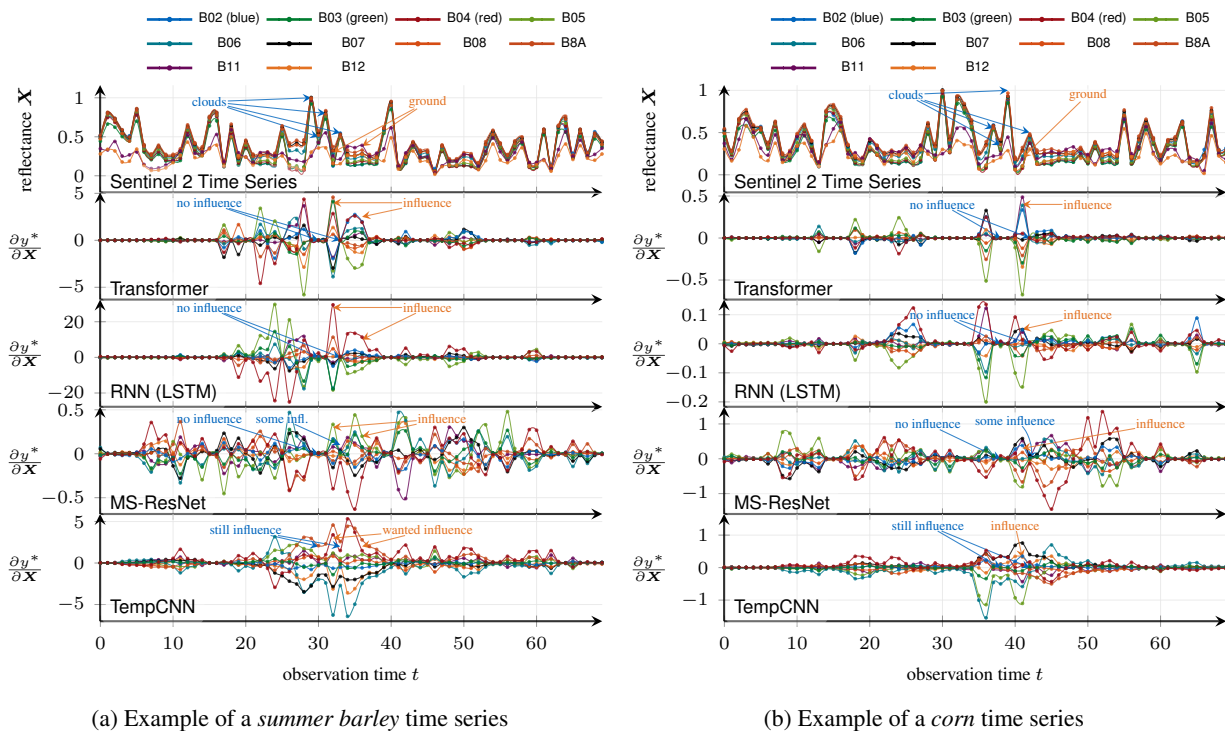


Figure 5: Input feature importance analysis by gradients of the input time series  $\mathbf{X}$

Deep learning models are differentiable functions  $f_{\Theta}$  that approximate a mapping from an input tensor  $\mathbf{X}$  to a ground truth tensor  $\mathbf{y}$ , as detailed in Section 3. In the training process, gradients are backpropagated using Eq. (1) in order to adjust the model weights  $\Theta$ . Since the model  $f_{\Theta}$  is fully differentiable, we can use the same mechanism to back-propagate gradients further up to the input tensor  $\mathbf{X}$ . When we start from the highest predicted score  $y^* = \max(\hat{\mathbf{y}})$ , we can propagate gradients through the entire network back to the individual elements  $\mathbf{x}_t = (x_t^{B01}, x_t^{B02}, x_t^{B03}, \dots)^T$  of the input tensor  $\mathbf{X} = (\mathbf{x}_0, \dots, \mathbf{x}_T)$ . These gradients  $\frac{\partial y^*}{\partial \mathbf{X}}$  reflect the influence of each input data element on the current class prediction. Vanishing gradients indicate that any change in the input has no effect on the prediction. Positive or negative gradients would suggest an increase or decrease of the predicted score if the input changed at these times. We would like to emphasize that this analysis is model-agnostic, can be implemented in few lines of code in current deep learning frameworks that utilize automatic differentiation, and does not require ground truth labels.<sup>5</sup>

For this experiment, we estimated the influence of each input time step on the classification prediction for each of the evaluated networks, *i.e.*, LSTM-RNN (recurrence) and Transformer (self-attention), as well as MS-ResNet and TempCNN (convolution). Figure 5 illustrates this by means of two separate examples of two corn- and summer barley parcels. The top figures each show the input time series  $\mathbf{X}$  as a sequence of raw Sentinel 2 reflectances over the year of 2018. In the raw time series, we can identify atmospheric noise and clouds as positive peaks in the data. These are caused by the high reflectance values of clouds throughout all spectral bands. The presence of a cloud at a given point in time does not provide any additional information about the covered surface and should be, thus, considered irrelevant for the classification. The following rows display the gradients  $\frac{\partial y^*}{\partial \mathbf{X}}$  for each of the respective models. These plots indicate the influence of the measurement at the particular input time in the top row on the classification prediction of the respective model.

The results of this experiment shows that the gradients through the LSTM-RNN and Transformer networks were only non-zero for comparatively few observations. This indicates that only a few key time-points are necessary to extract the classification relevant information from the raw time series. Only time points where the surface was not obscured by clouds had non-zero gradients. All cloudy observations did not influence the classification prediction, as

<sup>5</sup>Our implementation is available at <https://github.com/marccoru/crop-type-mapping/blob/master/notebooks/FeatureImportance.ipynb>

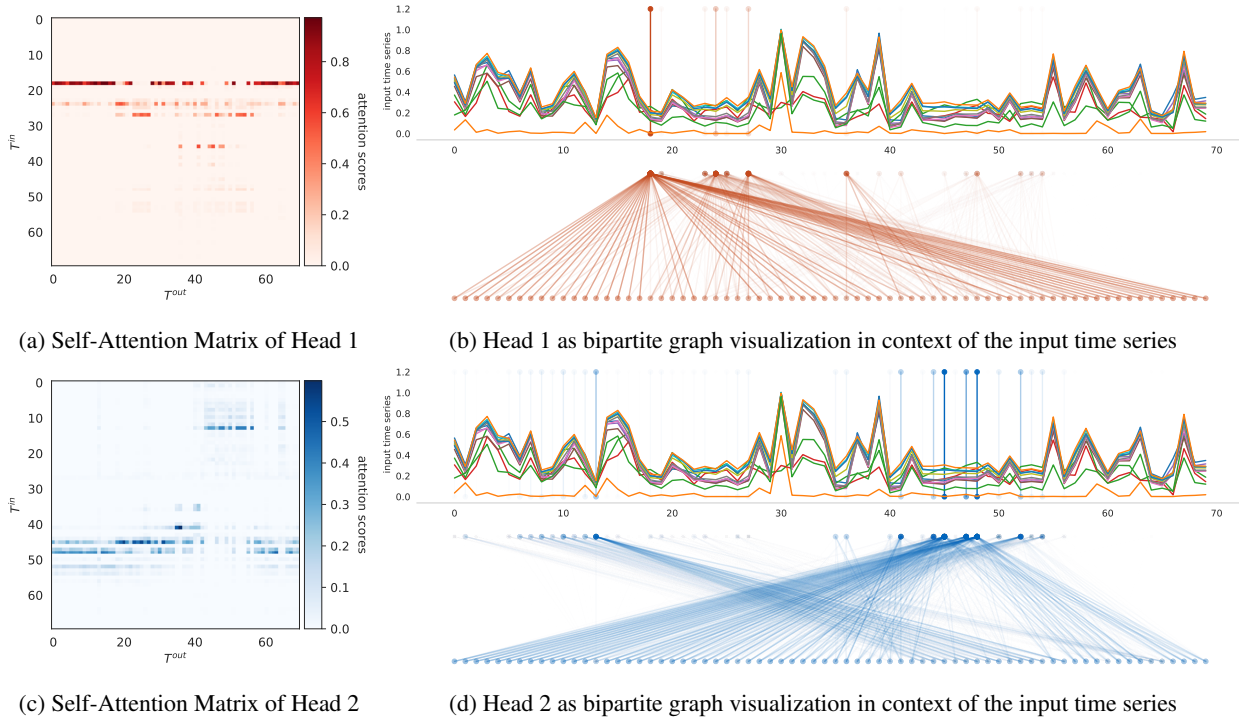


Figure 6: Visual illustration of the self-attention scores from a pre-trained transformer self-attention model

indicated by vanishing gradients. This experimentally shows that the LSTM-RNN and Transformer models have been optimized to automatically identify and suppress any cloudy time instances, learned purely from data.

The convolution-based model architectures MS-ResNet and TempCNN show, in general, a similar behavior. However, these models seem to have some non-zero gradients on cloudy observations. This is especially true for the comparatively shallow TempCNN architecture where the cloudy observations at  $t = 30$  in Fig. 5a and  $t = 38$  in Fig. 5b still have influence in the classification prediction. The MS-ResNet model also seems to be able to extract features from the entire temporal range. Since the data ranges from January to December, it is expected that the particular crop class is only visible during the summer periods. The MS-ResNet model seems to still include features from the winter periods.

Summarizing the above, the recurrence and self-attention based models LSTM-RNN and Transformer seem to extract selective temporal features, while the convolution-based models utilize the entire time series. Also, the LSTM-RNN and Transformer models were able to transition from a time observation with high gradients to zero gradients without any time delay. It appears that the convolution-based models TempCNN and MS-ResNet require at least two subsequent observations to reduce the influence of the particular time instance. This can be observed from Fig. 5a at  $t = 30$  and  $t = 34$ : The MS-ResNet model could reduce the influence of the observations at  $t = 30$  (indicated by zero gradients) when three subsequent observations were cloudy. However, when only one observation was cloudy, as in  $t = 34$ , MS-ResNet was unable to suppress this observation completely. In contrast, the models LSTM-RNN and Transformer were able to suppress these cloudy observations even if they appeared in a single time instance.

We attribute this difference in the influence of input observations to the respective mechanisms for feature extraction. Recurrent networks utilize internal gates that can control the influence of the particular time instance to a hidden memory state. Our previous work [51], which visualized internal LSTM states, supports this hypothesis for recurrence. Similarly, self-attention enables a model to select specific observations by assigning a large attention score to them. In contrast, convolutions always extract features from a local neighborhood. Hence, it seems to be more difficult for convolutional architectures to ignore sudden appearances of irrelevant observations within a temporal sequence, as indicated by the non-zero gradients at cloudy observations.

### 8.3. Qualitative Analysis of Self-Attention Scores

In the previous section, we experimentally observed that the Transformer model was able to suppress the influence of an observation for classification-irrelevant observations, *e.g.*, clouds. Here, we concentrate on the self-attention mechanism (*cf.* Section 3.4) that was implemented in the Transformer model and analyse the attention scores on the example of the cornfield parcels from the previous experiment in shown in Fig. 5b.

The Transformer models realize multi-headed self-attention which are essentially multiple attention mechanisms in parallel. To recall, every self-attention mechanism calculates an attention matrix  $\mathbf{A} \in [0, 1]^{T \times T}$  using the softmax operation following Eq. (3). These attention scores define the influence of an input time feature on a higher-level output time feature. We visualize the values of this matrix in Figs. 6a and 6c for two attention heads from the first self-attention layer. This matrix can be seen as an adjacency matrix between input nodes and output nodes. In Figs. 6b and 6d, we alternatively show the same matrix as bipartite graphs. The former matrix elements are now shown as weighted directed edges between input and output nodes. The strength of the attention is indicated by the opacity of the edge. Above the attention graph, we show the input time series of the example as a reference to allow for visual interpretation of the time instances. Here, the attention scores are drawn as vertical lines corresponding to the values in  $\mathbf{A}$ .

From these figures, we can directly observe that the self-attention scores focus on distinct events with each head. While the first head appears to focus on the first part of the time series, the second head observes features towards the later time series. Also, the attention scores seem to re-distribute features over time. Hence, even though hidden feature tensors throughout the network still maintain a temporal dimension, the temporal consistency with the input time series loses context. Consistent with the previous experiment in Section 8.2, we observed that the attention scores did not focus on the strong positive peaks in the time series which indicate a cloudy observation. Hence, we can conclude that self-attention mechanisms are a key tool in suppressing the non-classification-relevant cloudy observations which explain the zero-gradients of the previous experiment.

### 8.4. Feature Analyses with *t*-Distributed Stochastic Neighborhood Embedding (*t*-SNE)

Deep learning models, in general, extract features of increasingly complexity throughout the cascaded layer architectures [75]. In this experiment, we analyzed this property by visualizing the hidden features at varying deeper layers of the transformer architecture, as shown in Fig. 7. We reduced the initial feature dimensionality from  $D = 128$  to two visually interpretable dimensions using *t-distributed stochastic neighbor embedding (t-SNE)*[76]. This nonlinear dimensionality reduction technique estimates a source probability distribution over  $N = 30$  points (perplexity parameter) in the high-dimensional space and iteratively minimizes the *Kullback–Leibler* divergence between this and a target distribution in the two-dimensional output space. We used a trained transformer network with three self-attention layers and  $D = 128$  hidden dimensions. To obtain the features, we passed the entire test dataset over all regions through a pre-trained transformer network and recorded the hidden features after each self-attention layer and after the last dense layer before max pooling and softmax activation, as visualized in Fig. 7. The original features  $\mathbf{H} \in \mathbb{R}^{(T=70) \times (D=128)}$  were then averaged along the time dimension to obtain  $\mathbf{h}' \in \mathbb{R}^{D=128}$  and mapped into the final t-SNE space  $\mathbb{R}^{D=2}$ . The illustration shows the t-SNE representation of the embedded 200 samples for each of the 23 land use classes. We augmented the final plots with a key indicating the classes identities and a schematic illustration of the network topology. Since the class definitions are rather broad with, for instance, multiple categories of grassland, we grouped them by color but assigned varying marker shapes to each class. Note, that the t-SNE embedding only relies on the extracted features without taking the actual ground truth class label into account. One can easily observe that the transformed features become more and more separable with each deeper network layer. This becomes apparent by the formation clusters throughout the layers. Looking at the last dense layer, which is closest to the final prediction, we can identify distinct separable manifolds for corn (★) and rapeseed (☆). This suggests that these classes are well-separable in the feature space. The grassland (▶, ▲, ◆, ★) and fallow groups (★, ►) are located in direct vicinity to each other. This might be attributed to the observation that grass-like vegetation will grow naturally on parcels marked as unused/fallow. This fallow group itself also seems to share characteristics with beetroot (▶) and potatoe (▲), while peas (◆) form a separate cluster. The groups for winter crops (★, ▲, ◆, ●, ◆, ►) and summer crops (★, ▲, ◆, ►) appear precisely separated with distinct clusters within these groups between summer barley (►) and summer oat (▲). Interestingly, triticale, which originates from wheat and rye, seems to be separable depending on whether they are cultivated for biological gas production (GPS) (◆) or as regular triticale for consumption (●). Also, some parcels of other seemingly random classes have been embedded in the vicinity of well-defined clusters like corn (★) or rapeseed (☆). From expert knowledge provided by StMELF, we account for a certain degree of wrong labels in the dataset. The

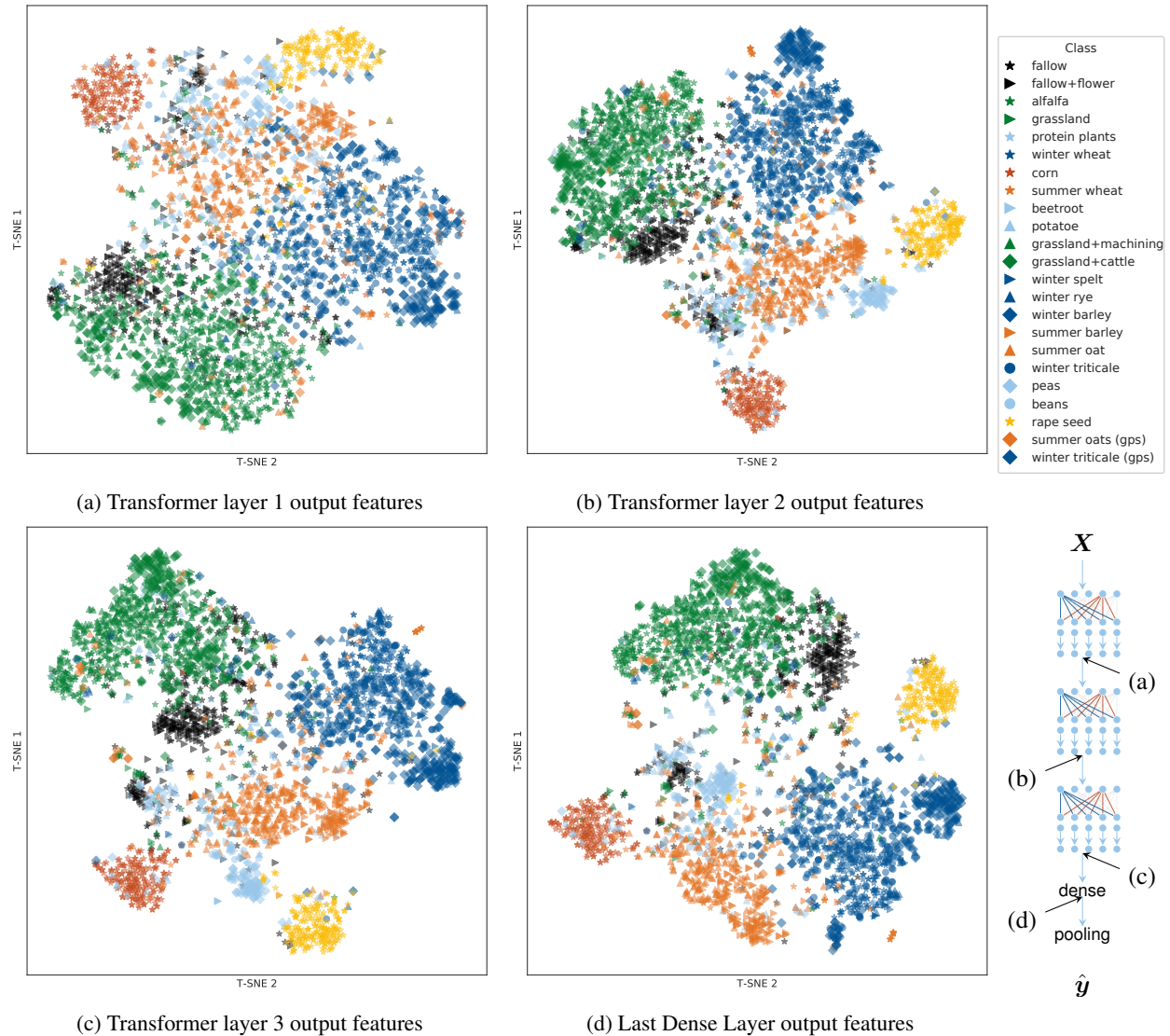


Figure 7: A t-SNE embedding of features encoded by a Transformer model

identification of these outliers is a key motivation for crop type monitoring. Hence, these few field parcels may have been assigned wrong labels by the respective farmer.

In summary, the feature extraction capabilities learned by this self-attention network is consistent with assumptions based on domain-knowledge of the particular classes. Methodologically, we observed that features from deeper cascaded network layers get increasingly distinctive and field parcels of the same label are mapped in similar embedded regions. We would like to stress that this type of analysis is not unique to self-attention networks and can be reproduced for many deep learning architectures that extracts features in cascaded layers<sup>6</sup>.

## 9. Conclusion

In this work, we quantitatively and qualitatively analyzed self-attention for the application in multi-temporal Earth observation. We performed a large-scale quantitative comparison in Section 8.1 where we evaluated multiple model architectures that rely on self-attention, recurrence and convolution, and a random forest baseline. We compared

<sup>6</sup>this analysis is available at <https://github.com/marccoru/crop-type-mapping/blob/master/notebooks/T-SNE.ipynb>

these models from multiple angles by reporting their performance on preprocessed and raw Sentinel 2 time series as well as land-use and a land-cover oriented set of classes. Here, we observed that all models performed equally well on preprocessed data. Even the random forest baseline achieved competitive overall accuracy. This leads to the conclusion that the choice of model architecture is less critical when extensive data preprocessing is utilized as a form of feature extraction aided by region-specific expert knowledge. For raw unprocessed Sentinel 2 time series data, the Transformer, and LSTM-RNN architectures were able to achieve better accuracies compared to the convolutional models. We investigated this further by a feature importance analysis in Section 8.2 using gradients where we observed that the mechanisms self-attention and recurrence helped to suppress non-classification-relevant observations in the time series. For the Transformer, this was realized by learning weights in the attention mechanism which enables the model to specifically focus on some observations, as could be observed in Fig. 1 in Section 8.3. Finally, we looked at the larger Transformer network topology and observed how deeper neural network layers were able to learn increasingly separable representations of the classes in Section 8.4. Since we chose a challenging set of classes, class overlaps in the semantic representation of classes with common properties were present and followed common intuition. This is a typical challenge for land cover and land use classification with long-tailed class distributions.

To summarize, we saw that self-attention is a promising technique that allows neural networks to extract features from specific time instances with raw optical satellite time series. It suits well in the canon of time series classification models that utilize recurrent or convolutional layers. We did not find any mechanism that systematically achieved better accuracies, but observed that self-attention and recurrence were, by design of the feature extraction, more robust to noise in the data and could better suppress cloudy observations in raw time series.

In the future, a robust classification of raw time series data without region-specific expert knowledge will be key to quantitatively exploit the satellite data that is published daily. We hope to have contributed a step towards this direction by this comprehensive study that evaluated model accuracies on preprocessed and raw data for a variety of mechanisms for time series classification.

## 10. Acknowledgements

We would like to thank Sabine Erbe from the Bavarian Ministry of Agriculture for the continuous and persistent support and valuable domain knowledge as well as Markus Ziegler and Christoph Schmidt from GAF-AG for their collaboration in the joint crop type classification project which provided objective, method and preprocessed time series data for this study. The work of Marc Rußwurm was funded by the *German Federal Ministry for Economic Affairs and Energy (BMWi)* under reference 50EE1908.

## References

- [1] Sentinel data access annual report 2019, date 06/05/19, COPE-SERCO-RP-19-0389 (2019).  
URL [https://scihub.copernicus.eu/twiki/pub/SciHubWebPortal/AnnualReport2018/COPE-SERCO-RP-19-0389\\_-\\_Sentinel\\_Data\\_Access\\_Annual\\_Report\\_Y2018\\_v1.0.pdf](https://scihub.copernicus.eu/twiki/pub/SciHubWebPortal/AnnualReport2018/COPE-SERCO-RP-19-0389_-_Sentinel_Data_Access_Annual_Report_Y2018_v1.0.pdf)
- [2] J. B. Odenweller, K. I. Johnson, Crop identification using Landsat temporal-spectral profiles, *Remote Sensing of Environment* 14 (1-3) (1984) 39–54. doi:10.1016/0034-4257(84)90006-3.
- [3] B. C. Reed, J. F. Brown, D. VanderZee, T. R. Loveland, J. W. Merchant, D. O. Ohlen, Measuring Phenological Variability from Satellite Imagery, *Journal of Vegetation Science* 5 (5) (1994) 703–714. doi:10.2307/3235884.  
URL <http://onlinelibrary.wiley.com/store/10.2307/3235884/asset/3235884.pdf?v=1&t=ijsra0qx&s=d6d17d000fc949bd7af1cccf70618a11f7f65c2c>
- [4] S. Foerster, K. Kaden, M. Foerster, S. Itzerott, Crop type mapping using spectral-temporal profiles and phenological information, *Computers and Electronics in Agriculture* 89 (2012) 30–40. doi:10.1016/j.compag.2012.07.015.  
URL <http://dx.doi.org/10.1016/j.compag.2012.07.015>
- [5] C. Conrad, S. Fritsch, J. Zeidler, G. Rücker, S. Dech, Per-Field Irrigated Crop Classification in Arid Central Asia Using SPOT and ASTER Data, *Remote Sensing* 2 (4) (2010) 1035–1056. doi:10.3390/rs2041035.  
URL <http://www.mdpi.com/2072-4292/2/4/1035/>

- [6] C. Conrad, S. Dech, O. Dubovyk, S. Fritsch, D. Klein, F. Löw, G. Schorcht, J. Zeidler, Derivation of temporal windows for accurate crop discrimination in heterogeneous croplands of Uzbekistan using multitemporal RapidEye images, *Computers and Electronics in Agriculture* 103 (2014) 63–74. doi:10.1016/j.compag.2014.02.003.  
URL <http://dx.doi.org/10.1016/j.compag.2014.02.003>
- [7] P. Hao, Y. Zhan, L. Wang, Z. Niu, M. Shakir, Feature Selection of Time Series MODIS Data for Early Crop Classification Using Random Forest: A Case Study in Kansas, USA, *Remote Sensing* 7 (5) (2015) 5347–5369. doi:10.3390/rs70505347.  
URL <http://www.mdpi.com/2072-4292/7/5/5347/>
- [8] J. M. Peña-Barragán, M. K. Ngugi, R. E. Plant, J. Six, Object-based crop identification using multiple vegetation indices, textural features and crop phenology, *Remote Sensing of Environment* 115 (6) (2011) 1301–1316. doi:10.1016/j.rse.2011.01.009.  
URL <http://linkinghub.elsevier.com/retrieve/pii/S0034425711000290>
- [9] L. Zhong, L. Hu, H. Zhou, Deep learning based multi-temporal crop classification, *Remote sensing of environment* 221 (2019) 430–443.
- [10] S. Valero, D. Morin, J. Inglada, G. Sepulcre, M. Arias, O. Hagolle, G. Dedieu, S. Bontemps, P. Defourny, B. Koetz, Production of a dynamic cropland mask by processing remote sensing image series at high temporal and spatial resolutions, *Remote Sensing* 8 (1) (2016) 1–21. doi:10.3390/rs8010055.
- [11] P. Kumar, D. K. Gupta, V. N. Mishra, R. Prasad, Comparison of support vector machine, artificial neural network, and spectral angle mapper algorithms for crop classification using LISS IV data, *International Journal of Remote Sensing* 36 (6) (2015) 1604–1617. doi:10.1080/2150704X.2015.1019015.
- [12] B. Zheng, S. W. Myint, P. S. Thenkabail, R. M. Aggarwal, A support vector machine to identify irrigated crop types using time-series landsat ndvi data, *International Journal of Applied Earth Observation and Geoinformation* 34 (2015) 103–112.
- [13] R. Devadas, R. Denham, M. Pringle, Support vector machine classification of object-based data for crop mapping, using multi-temporal landsat imagery, *Int. Arch. Photogramm. Remote Sens. Spat. Inf. Sci* 39 (2012) 185–190.
- [14] C. Ünsalan, K. L. Boyer, Review on Land Use Classification, in: *Multispectral Satellite Image Understanding: From Land Classification to Building and Road Detection*, Springer, 2011, pp. 49–64. doi:10.1007/978-0-85729-667-2\_5.
- [15] Y. Shao, R. S. Lunetta, Comparison of support vector machine, neural network, and cart algorithms for the land-cover classification using limited training data points, *ISPRS Journal of Photogrammetry and Remote Sensing* 70 (2012) 78–87.
- [16] P. Jönsson, L. Eklundh, Timesat—a program for analyzing time-series of satellite sensor data, *Computers & Geosciences* 30 (8) (2004) 833–845.
- [17] L. Eklundh, P. Jönsson, Timesat for processing time-series data from satellite sensors for land surface monitoring, in: *Multitemporal Remote Sensing*, Springer, 2016, pp. 177–194.
- [18] M. A. White, K. M. de Beurs, K. Didan, D. W. Inouye, A. D. Richardson, O. P. Jensen, J. O’KEEFE, G. Zhang, R. R. Nemani, W. J. van Leeuwen, et al., Intercomparison, interpretation, and assessment of spring phenology in north america estimated from remote sensing for 1982–2006, *Global Change Biology* 15 (10) (2009) 2335–2359.
- [19] L. Olsson, L. Eklundh, J. Ardö, A recent greening of the sahel—trends, patterns and potential causes, *Journal of Arid Environments* 63 (3) (2005) 556–566.
- [20] K. Jia, S. Liang, X. Wei, Y. Yao, Y. Su, B. Jiang, X. Wang, Land cover classification of landsat data with phenological features extracted from time series modis ndvi data, *Remote sensing* 6 (11) (2014) 11518–11532.
- [21] M. Singha, B. Wu, M. Zhang, An object-based paddy rice classification using multi-spectral data and crop phenology in assam, northeast india, *Remote Sensing* 8 (6) (2016) 479.

- [22] W. S. McCulloch, W. Pitts, A logical calculus of the ideas immanent in nervous activity, *The bulletin of mathematical biophysics* 5 (4) (1943) 115–133.
- [23] J. D. Cowan, Neural networks: the early days, in: *Advances in neural information processing systems*, 1990, pp. 828–842.
- [24] Y. LeCun, L. Bottou, Y. Bengio, P. Haffner, et al., Gradient-based learning applied to document recognition, *Proceedings of the IEEE* 86 (11) (1998) 2278–2324.
- [25] J. Deng, W. Dong, R. Socher, L.-J. Li, K. Li, L. Fei-Fei, Imagenet: A large-scale hierarchical image database, in: *2009 IEEE conference on computer vision and pattern recognition*, IEEE, 2009, pp. 248–255.
- [26] O. Russakovsky, J. Deng, H. Su, J. Krause, S. Satheesh, S. Ma, Z. Huang, A. Karpathy, A. Khosla, M. Bernstein, et al., Imagenet large scale visual recognition challenge, *International journal of computer vision* 115 (3) (2015) 211–252.
- [27] K. Simonyan, A. Zisserman, Very deep convolutional networks for large-scale image recognition, arXiv preprint arXiv:1409.1556.
- [28] A. Krizhevsky, I. Sutskever, G. E. Hinton, Imagenet classification with deep convolutional neural networks, in: *Advances in neural information processing systems*, 2012, pp. 1097–1105.
- [29] K. He, X. Zhang, S. Ren, J. Sun, Deep residual learning for image recognition, in: *Proceedings of the IEEE conference on computer vision and pattern recognition*, 2016, pp. 770–778.
- [30] J. Long, E. Shelhamer, T. Darrell, Fully convolutional networks for semantic segmentation, in: *Proceedings of the IEEE conference on computer vision and pattern recognition*, 2015, pp. 3431–3440.
- [31] C. Szegedy, S. Ioffe, V. Vanhoucke, A. A. Alemi, Inception-v4, inception-resnet and the impact of residual connections on learning, in: *Thirty-First AAAI Conference on Artificial Intelligence*, 2017.
- [32] A. Vaswani, N. Shazeer, N. Parmar, J. Uszkoreit, L. Jones, A. N. Gomez, Ł. Kaiser, I. Polosukhin, Attention is all you need, in: *Advances in neural information processing systems*, 2017, pp. 5998–6008.
- [33] J. Devlin, M.-W. Chang, K. Lee, K. Toutanova, Bert: Pre-training of deep bidirectional transformers for language understanding, arXiv preprint arXiv:1810.04805.
- [34] A. Radford, J. Wu, R. Child, D. Luan, D. Amodei, I. Sutskever, Language models are unsupervised multitask learners, *OpenAI Blog* 1 (8).
- [35] D. Marmanis, M. Datcu, T. Esch, U. Stilla, Deep learning earth observation classification using imagenet pre-trained networks, *IEEE Geoscience and Remote Sensing Letters* 13 (1) (2015) 105–109.
- [36] M. Volpi, D. Tuia, Dense semantic labeling of subdecimeter resolution images with convolutional neural networks, *IEEE Transactions on Geoscience and Remote Sensing* 55 (2) (2016) 881–893.
- [37] J. Sherrah, Fully convolutional networks for dense semantic labelling of high-resolution aerial imagery, arXiv preprint arXiv:1606.02585.
- [38] N. Audebert, B. Le Saux, S. Lefèvre, Semantic segmentation of earth observation data using multimodal and multi-scale deep networks, in: *Asian conference on computer vision*, Springer, 2016, pp. 180–196.
- [39] M. Rußwurm, M. Korner, Temporal vegetation modelling using long short-term memory networks for crop identification from medium-resolution multi-spectral satellite images, in: *Proceedings of the IEEE Conference on Computer Vision and Pattern Recognition Workshops*, 2017, pp. 11–19.
- [40] X. Jia, A. Khandelwal, G. Nayak, J. Gerber, K. Carlson, P. West, V. Kumar, Incremental Dual-memory LSTM in Land Cover Prediction, in: *23rd ACM SIGKDD International Conference on Knowledge Discovery and Data Mining*, 2017, pp. 867–876. doi:10.1145/3097983.3098112.  
URL <http://dl.acm.org/citation.cfm?doid=3097983.3098112>

- [41] H. Lyu, H. Lu, L. Mou, Learning a Transferable Change Rule from a Recurrent Neural Network for Land Cover Change Detection, *Remote Sensing* 8 (12) (2016) 506. doi : 10.3390/rs8060506.  
URL <http://www.mdpi.com/2072-4292/8/6/506>
- [42] L. Mou, L. Bruzzone, X. X. Zhu, Learning Spectral-Spatial-Temporal Features via a Recurrent Convolutional Neural Network for Change Detection in Multispectral Imagery, *Arxiv* arXiv:1803.02642.  
URL <http://arxiv.org/abs/1803.02642>
- [43] P. Benedetti, D. Ienco, R. Gaetano, K. Ose, R. G. Pensa, S. Dupuy, M3fusion: A deep learning architecture for multiscale multimodal multitemporal satellite data fusion, *IEEE Journal of Selected Topics in Applied Earth Observations and Remote Sensing* 11 (12) (2018) 4939–4949.
- [44] R. Interdonato, D. Ienco, R. Gaetano, K. Ose, Duplo: A dual view point deep learning architecture for time series classification, *ISPRS journal of photogrammetry and remote sensing* 149 (2019) 91–104.
- [45] P. J. Werbos, Backpropagation through time: what it does and how to do it, *Proceedings of the IEEE* 78 (10) (1990) 1550–1560.
- [46] S. Hochreiter, J. Schmidhuber, Long Short-Term Memory, *Neural Computation* 9 (8) (1997) 1735–1780. doi : 10.1162/neco.1997.9.8.1735.
- [47] J. Chung, C. Gulcehre, K. Cho, Y. Bengio, Empirical evaluation of gated recurrent neural networks on sequence modeling, *arXiv preprint arXiv:1412.3555*.
- [48] I. Sutskever, O. Vinyals, Q. V. Le, Sequence to sequence learning with neural networks, in: *Advances in neural information processing systems*, 2014, pp. 3104–3112.
- [49] V. S. F. Garnot, L. Landrieu, S. Giordano, N. Chehata, Time-space tradeoff in deep learning models for crop classification on satellite multi-spectral image time series, *arXiv preprint arXiv:1901.10503*.
- [50] A. Sharma, X. Liu, X. Yang, Land cover classification from multi-temporal, multi-spectral remotely sensed imagery using patch-based recurrent neural networks, *Neural Networks* 105 (2018) 346–355.
- [51] M. Rußwurm, M. Körner, Multi-temporal land cover classification with sequential recurrent encoders, *ISPRS International Journal of Geo-Information* 7 (4) (2018) 129.
- [52] D. Bahdanau, J. Chorowski, D. Serdyuk, P. Brakel, Y. Bengio, End-to-end attention-based large vocabulary speech recognition, in: *2016 IEEE international conference on acoustics, speech and signal processing (ICASSP)*, IEEE, 2016, pp. 4945–4949.
- [53] H. I. Fawaz, G. Forestier, J. Weber, L. Idoumghar, P.-A. Muller, Deep learning for time series classification: a review, *Data Mining and Knowledge Discovery* 33 (4) (2019) 917–963.
- [54] C. Pelletier, G. I. Webb, F. Petitjean, Temporal convolutional neural network for the classification of satellite image time series, *Remote Sensing* 11 (5) (2019) 523.
- [55] D. E. Rumelhart, G. E. Hinton, R. J. Williams, Learning representations by back-propagating errors, *Nature* 323 (6088) (1986) 533–536. doi:10.1038/323533a0.  
URL <http://www.nature.com/doifinder/10.1038/323533a0>
- [56] R. Jozefowicz, W. Zaremba, I. Sutskever, An Empirical Exploration of Recurrent Network Architectures, in: *Proceedings of the 32nd International Conference on Machine Learning (ICML-15)*, 2015, pp. 2342–2350. arXiv:1512.03385.
- [57] B. Yoshua, S. Patrice, F. Paolo, Learning long-term dependencies with gradient descent is difficult, *IEEE transactions on neural networks* 5 (2) (1994) 157–166.
- [58] R. Jozefowicz, W. Zaremba, I. Sutskever, An empirical exploration of recurrent network architectures, in: *International Conference on Machine Learning*, 2015, pp. 2342–2350.

- [59] H. Ismail Fawaz, B. Lucas, G. Forestier, C. Pelletier, D. F. Schmidt, J. Weber, G. I. Webb, L. Idoumghar, P.-A. Muller, F. Petitjean, Inceptiontime: Finding alexnet for time series classification, ArXiv.
- [60] N. Hatami, Y. Gavet, J. Debayle, Classification of time-series images using deep convolutional neural networks, in: Tenth International Conference on Machine Vision (ICMV 2017), Vol. 10696, International Society for Optics and Photonics, 2018, p. 106960Y.
- [61] S. Ioffe, C. Szegedy, Batch normalization: Accelerating deep network training by reducing internal covariate shift, arXiv preprint arXiv:1502.03167.
- [62] Z. Wang, W. Yan, T. Oates, Time series classification from scratch with deep neural networks: A strong baseline, in: 2017 international joint conference on neural networks (IJCNN), IEEE, 2017, pp. 1578–1585.
- [63] Z. Cui, W. Chen, Y. Chen, Multi-scale convolutional neural networks for time series classification, arXiv preprint arXiv:1603.06995.
- [64] H. A. Dau, A. Bagnall, K. Kamgar, C.-C. M. Yeh, Y. Zhu, S. Gharghabi, C. A. Ratanamahatana, E. Keogh, The ucr time series archive, arXiv preprint arXiv:1810.07758.
- [65] A. Bagnall, H. A. Dau, J. Lines, M. Flynn, J. Large, A. Bostrom, P. Southam, E. Keogh, The uea multivariate time series classification archive, 2018, arXiv preprint arXiv:1811.00075.
- [66] F. Pedregosa, G. Varoquaux, A. Gramfort, V. Michel, B. Thirion, O. Grisel, M. Blondel, P. Prettenhofer, R. Weiss, V. Dubourg, et al., Scikit-learn: Machine learning in python, Journal of machine learning research 12 (Oct) (2011) 2825–2830.
- [67] D. P. Kingma, J. Ba, Adam: A method for stochastic optimization, arXiv preprint arXiv:1412.6980.
- [68] J. Cohen, A coefficient of agreement for nominal scales, Educational and Psychological Measurement 20 (1960) 37–46.  
URL <ftp://gis.msl.mt.gov/Maxell/Models/Predictive{ }Modeling{ }for{ }DSS{ }Lincoln{ }NEModeling{ }Literature/Cohen{ }1960.pdf>
- [69] J. Bergstra, D. Yamins, D. D. Cox, Hyperopt: A python library for optimizing the hyperparameters of machine learning algorithms, in: Proceedings of the 12th Python in science conference, Citeseer, 2013, pp. 13–20.
- [70] L. Li, K. Jamieson, A. Rostamizadeh, E. Gonina, M. Hardt, B. Recht, A. Talwalkar, Massively parallel hyperparameter tuning, arXiv preprint arXiv:1810.05934.
- [71] R. Liaw, E. Liang, R. Nishihara, P. Moritz, J. E. Gonzalez, I. Stoica, Tune: A research platform for distributed model selection and training, arXiv preprint arXiv:1807.05118.
- [72] P. Schratz, J. Muenchow, E. Iturritxa, J. Richter, A. Brenning, Performance evaluation and hyperparameter tuning of statistical and machine-learning models using spatial data, arXiv preprint arXiv:1803.11266.
- [73] A. Brenning, Spatial cross-validation and bootstrap for the assessment of prediction rules in remote sensing: The r package sperrorest, in: 2012 IEEE international geoscience and remote sensing symposium, IEEE, 2012, pp. 5372–5375.
- [74] N. Gorelick, M. Hancher, M. Dixon, S. Ilyushchenko, D. Thau, R. Moore, Google earth engine: Planetary-scale geospatial analysis for everyone, Remote Sensing of Environment 202 (2017) 18–27.
- [75] I. Goodfellow, Y. Bengio, A. Courville, Deep learning, MIT press, 2016.
- [76] L. v. d. Maaten, G. Hinton, Visualizing data using t-sne, Journal of machine learning research 9 (Nov) (2008) 2579–2605.